PHYSICAL REVIEW MATERIALS **1**, 051601(R) (2017)

Quantum twin spectra in nanocrystalline silicon

Takahiro Matsumoto,[1,2,*] Takashi Ohhara,[3] Hidehiko Sugimoto,[4] Stephen M. Bennington,[5] and Susumu Ikeda[6]

[1]*Graduate School of Design and Architecture, Nagoya City University, Nagoya 464-0083, Japan*

[2]*Graduate School of Medical Sciences, Nagoya City University, Nagoya 464-0083, Japan*

[3]*Neutron Science Section, J-PARC Center, Japan Atomic Energy Agency, Ibaraki 319-1195, Japan*

[4]*Department of Physics, Faculty of Science and Engineering, Chuo University, Tokyo 112-8551, Japan*

[5]*ISIS Facility, Rutherford Appleton Laboratory, Chilton, Didcot OX11 0QX, United Kingdom*

[6]*High Energy Accelerator Research Organization, Ibaraki 319-1195, Japan*

(Received 15 May 2017; revised manuscript received 23 July 2017; published 10 October 2017)

Using inelastic neutron-scattering spectroscopy, we have identified twin-split scattering spectra in hydrogen-terminated nanocrystalline silicon. We show that this duality originates from the cooperative motion of hydrogen and silicon. Our formalism for the inelastic neutron-scattering spectrum, which is derived from the Hermite orthogonal wave functions in terms of the normal coordinates, elucidates the physical origin of the observed quantum twin spectra and predicts the possible occurrence of this behavior in other materials such as metal hydrides.

DOI: 10.1103/PhysRevMaterials.1.051601

Hydrogen plays an important role in the fabrication of semiconductor devices such as in the passivation of defects and dangling bonds [1–3]. These features are deeply related to the degradation of silicon devices, e.g., by increasing the threshold voltage in metal oxide transistors [4,5], reducing the photoconduction in hydrogenated amorphous silicon solar cells, which is known as the Staebler-Wronski effect [6,7], and reducing the luminescence efficiency in nanocrystalline silicon (n-Si) [8–12].

The stability of hydrogen-passivated materials depends not only on the bonding energy between silicon and hydrogen but also on the vibrational frequency and the overlap of the hydrogen wave functions with adjacent atoms. From an experimental viewpoint, high-resolution electron energy loss spectroscopy (HREELS) [13,14], infrared absorption, and Raman spectroscopy [15–17] were used to clarify the dynamical properties of the hydrogenated silicon surface. In addition, theoretical calculations for the surface structure and lattice vibrations of the hydrogenated silicon system were performed using a semiempirical approach [18,19] and *ab initio* methods [20–22].

The measured vibrational energy levels using the above spectroscopic techniques (e.g., HREELS, infrared absorption, and Raman spectroscopy) cannot fully exploit the dynamics of the hydrogen nuclei because these spectroscopic techniques probe charge distributions surrounding the nuclei caused by Coulomb interactions. On the other hand, uncharged neutrons primarily interact with the nucleus itself and are scattered by nuclear forces (Fermi pseudopotential [23]). Therefore, neutrons can probe nuclear information inside the electron cloud [24,25].

Other advantageous features of the use of neutrons is their strong scattering by hydrogen nuclei. For example, the neutron-scattering cross section for protons is one to two orders of magnitude larger than that for any other atom [26], and the scattering intensity is related to the mean-square amplitude of the displacement scaled by the nuclear cross section for each atom. Another advantageous feature, in addition to this strong scattering property, is that the energy of thermal neutrons is of the same order as the vibrational energies, so when a neutron is inelastically scattered by the phonons and vibrations, the observed change in the energy of the neutron is a large fraction of its initial energy. Hence, neutron spectroscopies [27–31] provide crucial information on the vibrational dynamics of hydrogen nuclei helping to understand the degradation [6–12] and giant isotope mechanisms [32,33].

Here, using incoherent inelastic neutron-scattering (INS) spectroscopy, we elucidate the dynamics of hydrogen terminating the surface of n-Si in detail. We observed two split scattering spectra in the three-dimensional neutron-scattering contour maps [scattering intensity (S), energy ($\hbar\omega$), and momentum-transfer (Q) axis], and it is found that these two spectra have twin spectral characteristics; here, we define the twin spectra as spectra at different energy levels with a constant intensity ratio for any momentum-transfer axis. This twin spectral characteristic is not explained by a standard neutron analysis based on the scattering from single atoms (hydrogen nuclei) [34,35]. We therefore establish a quantum double oscillator (QDO) model based on the cooperative motion of hydrogen and silicon. We quantitatively describe this twin spectral characteristic as the product of the harmonic oscillators expressed in normal coordinates that are obtained by diagonalizing the displacement coordinates for both Si and H.

INS measurements were performed on a time-of-flight MARI chopper spectrometer at ISIS (ISIS Facility, Rutherford Appleton Laboratory). The incident energy E_i was varied from 0.1 to 1 eV with a resolution of $\Delta E_i/E_i \cong 2\%$. We measured the $S(Q,\omega)$ contour maps for both n-Si and bulk Si crystals. For the n-Si measurement, 1 g of powdered n-Si fabricated by electrochemical anodization [36–38] was wrapped in aluminum foil and rolled into a cylindrical shape to minimize the extinction effect. The average diameter of n-Si was 2.4 nm as evaluated by small-angle x-ray scattering measurements [38]. Then, this sample was enclosed in a cylindrical aluminum sample cell. For the bulk Si crystal measurement, 10 g of powdered Si crystals (0.1–0.2 mm in diameter) was placed on the MARI spectrometer, and the

*Corresponding author: matsumoto@sda.nagoya-cu.ac.jp

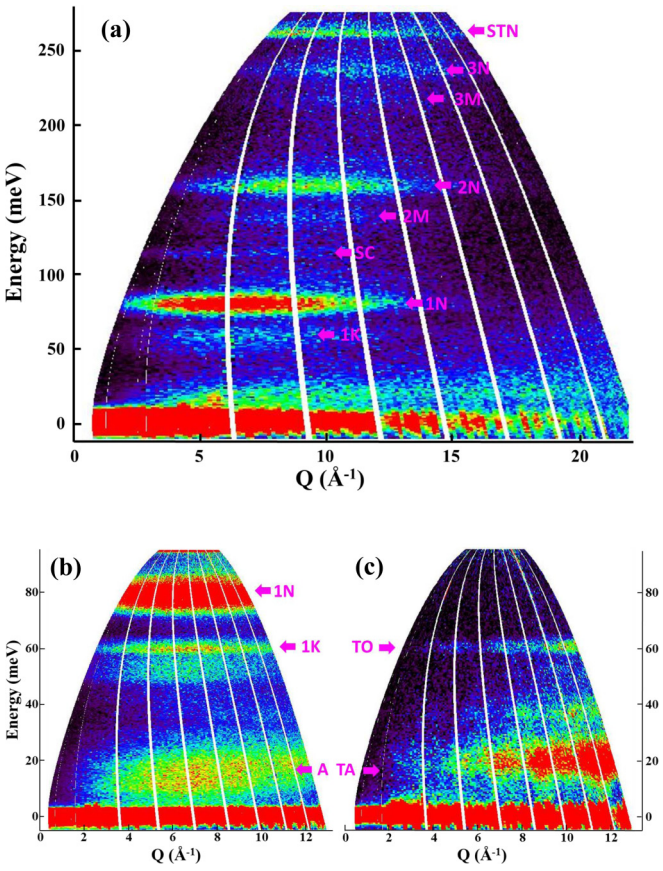

FIG. 1. $S(Q,\omega)$ contour maps for n-Si [(a) and (b)] and bulk Si [(c)] as measured by INS. The energy of the incident neutron is (a) $E_i = 300$ meV, (b) $E_i = 100$ meV, and (c) $E_i = 100$ meV. The obtained energy states are 1K = 59.2 meV, 1N = 81.2 meV, 2M = 137.6 meV, 2N = 158.8 meV, 3M = 217.1 meV, 3N = 236.5 meV, and STN = 261.2 meV. Other energy states such as $A = 15-20$ meV (acoustic Si phonons) and SC = 114.7 meV (scissor mode) are also observed. Each energy state (denoted by 1, 2, and 3) is split into two states with identical momentum-transfer dependences, as shown in the contour map. (b) Phonon energies of n-Si observed through the hydrogen motion. (c) Phonon energies of the bulk Si. A comparison of (b) and (c) shows that the Si phonon dynamics can be observed via scattering from the H nucleus. For example, the energy of the 1K state corresponds to the LO and TO phonon states, and the A state corresponds to the LA and TA phonon states. However, the 1K state peaks at $Q = 6.5$ Å^{-1}, whereas the LO and TO phonon states peak beyond $Q \geqslant 13$ Å^{-1}.

measurements were performed following the procedure of the n-Si measurements.

Figure 1 shows the INS data of the n-Si and bulk Si. Figures 1(a)–1(c) show contour maps of the scattering intensity, $S(Q,\omega)$ as a function of momentum transfer Q, and the energy $\hbar\omega$ for n-Si [(a) and (b)] and bulk Si [(c)]. Here, the momentum transfer vector $\mathbf{Q}$ is defined as $\mathbf{Q} = \mathbf{k_i} - \mathbf{k_f}$ ($Q = |\mathbf{k_i} - \mathbf{k_f}|$) with $k_i = 2\pi/\lambda_i$ and $k_f = 2\pi/\lambda_f$, where λ_i and λ_f are the incident and scattered wavelengths, respectively. The neutron energy transfer is $E = \hbar\omega$. The energy of the incident neutron was (a) $E_i = 300$ meV, (b) $E_i = 100$ meV, and (c) $E_i = 100$ meV. Dispersionless spectra that originate from Si-H vibrations are clearly observed in the $S(Q,\omega)$ contour maps.

First, we consider the spectra of the scattering intensity as a function of energy $S(\omega)$. Inelastic scattering peaks appeared at the energy levels of $\hbar\omega = 59.2$ meV (1K), 81.2 meV (1N), 114.7 meV (SC), 137.6 meV (2M), 158.8 meV (2N), 217.1 meV (3M), 236.5 meV (3N), and 261.2 meV (STN), as indicated by pink arrows in Fig. 1(a). The characteristic feature of the contour map is the presence of two split energy levels with identical Q-dependent peak position and an energy difference of approximately 20 meV, e.g., 1N − 1K = 2N − 2M = 3N − 3M = 20 meV. Furthermore, the energy difference between the higher number state and the lower number state is nearly equal to 78 meV; for example, 3N − 2N = 2N − 1N = 3M − 2M = 2M − 1K = 78 meV. The experimental results for the equally separated energy states with the two split energy levels are not explained by a standard neutron analysis based on the scattering from single atoms (hydrogen nuclei) [34,35].

Second, the energy of the $1K$ state of n-Si coincides with the energy of the LO and TO phonon states of bulk Si [39]. However, the momentum-transfer dependence (Q dependence) is different, as shown in Figs. 1(b) (n-Si) and 1(c) (bulk Si). For example, the energy of the 1K state corresponds to the LO and TO phonon states, and the A state corresponds to the LA and TA phonon states. However, the peak position of the 1K state is at $Q = 6.5$ Å^{-1}, whereas the peak positions of the LO and TO phonon states are beyond $Q \geqslant 13$ Å^{-1} ($Q = 28$ Å^{-1}, as estimated by the QDO model). This result shows that the 1K state contains information on the LO and TO phonon dynamics for n-Si and can be observed via scattering from the Si and H nuclei.

The hydrogen dynamics in coordination with the Si motion are quantitatively described by the QDO model, as shown in Fig. 2. The model represents lateral vibrations in the X-Y plane (bending motion) and longitudinal vibrations in the Z axis (stretching motion). Here, the position of each atom (Si: $\mathbf{r_1}$ and H: $\mathbf{r_2}$) may be expressed by introducing displacement vectors $\mathbf{u_1} = (u_{1X}, u_{1Y}, u_{1Z})$ and $\mathbf{u_2} = (u_{2X}, u_{2Y}, u_{2Z})$ from the equilibrium positions $\mathbf{R_1}$ and $\mathbf{R_2}$: $\mathbf{r_1} = \mathbf{u_1} + \mathbf{R_1}$ and $\mathbf{r_2} = \mathbf{u_2} + \mathbf{R_2}$, where subscript 1 indicates Si and subscript 2 indicates H.

Newton's equations of motion for both Si and H vibrations from the equilibrium positions may be written as

$$\mu_1 \frac{d^2 u_{1\rho}}{dt^2} = -\kappa_{1\rho}\, u_{1\rho} + \kappa_{2\rho}\,(u_{2\rho} - u_{1\rho}), \quad (1)$$

$$\mu_2 \frac{d^2 u_{2\rho}}{dt^2} = -\kappa_{2\rho}\,(u_{2\rho} - u_{1\rho}), \quad (2)$$

where the Si and H masses are defined as μ_1 and μ_2, and the force constants for the Si-Si and Si-H bonds are given as $\kappa_{1\rho}$ and $\kappa_{2\rho}$, respectively, where ρ denotes the X, Y, or Z coordinates. Here, we assume that the anharmonicity is negligibly small based on the experimental results of the equally separated energy states shown in Fig. 1(a).

The above diagonalization procedure for the equations of motion gives a set of six components for the orthogonal

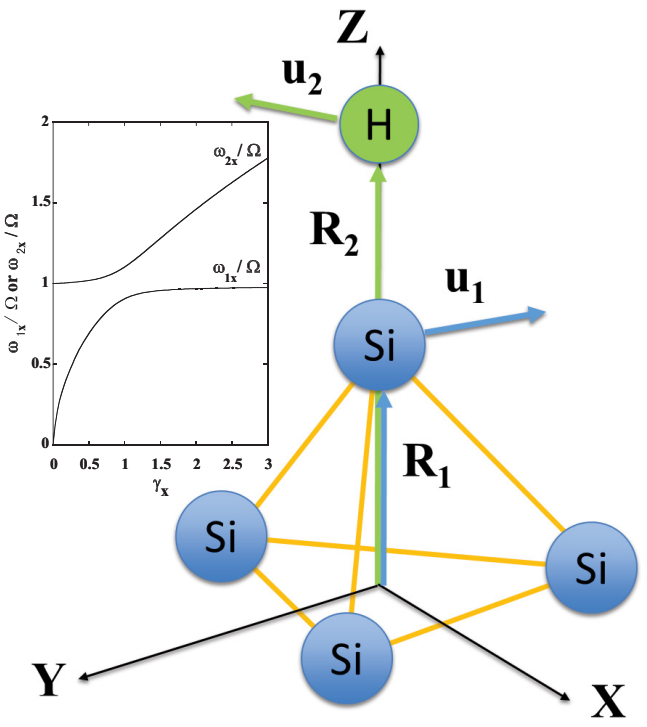

FIG. 2. QDO model for the description of hydrogen dynamics with the silicon motion. The position of each atom (Si: $\mathbf{r_1}$ and H: $\mathbf{r_2}$) is expressed by the displacement vectors $\mathbf{u_1}$ and $\mathbf{u_2}$ from the equilibrium positions $\mathbf{R_1}$ and $\mathbf{R_2}$ as $\mathbf{r_1} = \mathbf{u_1} + \mathbf{R_1}$ and $\mathbf{r_2} = \mathbf{u_2} + \mathbf{R_2}$, where subscript 1 indicates Si, and subscript 2 indicates H. The Si and H masses are defined as μ_1 and μ_2, respectively. The force constants for the Si-Si and Si-H bonds are expressed as $\kappa_{1\rho}$ and $\kappa_{2\rho}$, respectively, while ρ denotes the X, Y, or Z coordinates. The inset shows the eigenvalue frequency curves of the normal mode, $\omega_{\nu\rho}/\Omega_\rho$, to determine the ratio $\gamma_\rho = [(\kappa_{2\rho}/\mu_2)/(\kappa_{1\rho}/\mu_1)]$. Here, the dispersion curves for $\rho = X$ are drawn for clarity.

harmonic oscillators described by the normal coordinate $\xi_{\nu\rho}$ (see Supplemental Material S1 [40]). The Schrödinger equation described by the normal coordinate takes the following form:

$$\sum_{\nu=1}^{2}\sum_{\rho=X}^{Z}\left(-\frac{\hbar^2}{2}\frac{\partial^2}{\partial\,\xi_{\nu\rho}^2}+\frac{1}{2}\omega_{\nu\rho}^2\,\xi_{\nu\rho}^2\right)\Psi(\xi_{1X},\,\xi_{2X},\,\ldots,\xi_{2Z}) = E\,\Psi(\xi_{1X},\,\xi_{2X},\ldots,\xi_{2Z}), \tag{3}$$

where $\omega_{\nu\rho}$ is the eigenvalue frequency obtained by the diagonalization procedure (see Supplemental Material S1 [40]), E is the energy eigenvalue. and $\Psi(\xi_{1X},\,\ldots,\xi_{2Z})$ is the wave function of the eigenstate.

The wave function $\Psi(\xi_{1X},\,\ldots,\xi_{2Z})$ is described by the product of the harmonic oscillator wave functions $\Phi_{n_{\nu\rho}}(\xi_{\nu\rho})$ as

$$\begin{aligned}\Psi(\xi_{1x},\,\ldots,\xi_{2z}) &= \prod_{\nu\,=\,1}^{2}\prod_{\rho\,=\,X}^{Z}\Phi_{n_{\nu\rho}}(\xi_{\nu\rho})\\ &= \prod_{\nu\,=\,1}^{2}\prod_{\rho\,=\,X}^{Z}\frac{1}{\left(\sqrt{\pi}\,2^{n_{\nu\rho}}n_{\nu\rho}!\,\chi_{\nu\rho}\right)^{1/2}}\\ &\quad\times\exp\left[-\frac{1}{2}\left(\frac{\xi_{\nu\rho}}{\chi_{\nu\rho}}\right)^2\right]\mathrm{H}_{n_{\nu\rho}}\left(\frac{\xi_{\nu\rho}}{\chi_{\nu\rho}}\right),\end{aligned} \tag{4}$$

with the energy eigenvalue E as

$$E=\sum_{\nu=1}^{2}\sum_{\rho=X}^{Z}\left(n_{\nu\rho}+\frac{1}{2}\right)\hbar\omega_{\nu\rho}, \tag{5}$$

where $n_{\nu\rho}$ is the quantum number, $\chi_{\nu\rho} = \sqrt{\hbar/\omega_{\nu\rho}}$, $\mathrm{H}_{n_{\nu\rho}}$ is the Hermite polynomial with the number $n_{\nu\rho}$, and the energy eigenvalue E is expressed by the sum of the frequency of each normal mode.

Based on the results obtained from Eq. (5), we can compare the experimentally observed energies to the theoretically obtained values. The experimentally observed spectral energy states (indicated by arrows) in Fig. 1(a) can be assigned using the set of quantum numbers in Table I. Based on the symmetry of the model in Fig. 2, the lateral vibration in the X-Y plane

TABLE I. Energy states obtained from the INS data (first row), experimentally determined energy levels (second row), theoretically determined energy levels (third row), experimentally determined ratios (fourth row), theoretically determined ratios (fifth row), and the set of quantum numbers for a given energy state (sixth row). The possible combinations for each set of quantum numbers are described in algebraic form.

Energy level	Observed energy (meV)	Estimated energy (meV)	Observed ratio	Estimated ratio	Set of quantum numbers
1N	81.2	79.4	1	1	$n_{2X}+n_{2Y}=1,\ n_{1X}=n_{1Y}=n_{1Z}=n_{2Z}=0$
1K	59.2	59.4	0.33	0.32	$n_{1X}+n_{1Y}=1,\ n_{2X}=n_{2Y}=n_{1Z}=n_{2Z}=0$
2N	158.8	158.8	1	1	$n_{2X}+n_{2Y}=2,\ n_{1X}=n_{1Y}=n_{1Z}=n_{2Z}=0$
2M	137.6	138.8	0.53	0.53	$n_{1X}+n_{1Y}=1,\ n_{2X}+n_{2Y}=1,\ n_{1Z}=n_{2Z}=0$
2K	NA	118.8	NA	0.07	$n_{1X}+n_{1Y}=2,\ n_{2X}=n_{2Y}=n_{1Z}=n_{2Z}=0$
3N	236.5	238.2	1	1	$n_{2X}+n_{2Y}=3,\ n_{1X}=n_{1Y}=n_{1Z}=n_{2Z}=0$
3M	217.1	218.2	0.77	0.81	$n_{1X}+n_{1Y}=1,\ n_{2X}+n_{2Y}=2,\ n_{1Z}=n_{2Z}=0$
3L	NA	199.6	NA	0.2	$n_{1X}+n_{1Y}=2,\ n_{2X}+n_{2Y}=1,\ n_{1Z}=n_{2Z}=0$
3K	NA	178.2	NA	0.02	$n_{1X}+n_{1Y}=3,\ n_{2X}=n_{2Y}=n_{1Z}=n_{2Z}=0$
STN	261.2	261.2	1	1	$n_{2Z}=1,\ n_{1X}=n_{2X}=n_{1Y}=n_{2Y}=n_{1Z}=0$
STK	NA	61	NA	0.16	$n_{1Z}=1,\ n_{1X}=n_{2X}=n_{1Y}=n_{2Y}=n_{2Z}=0$

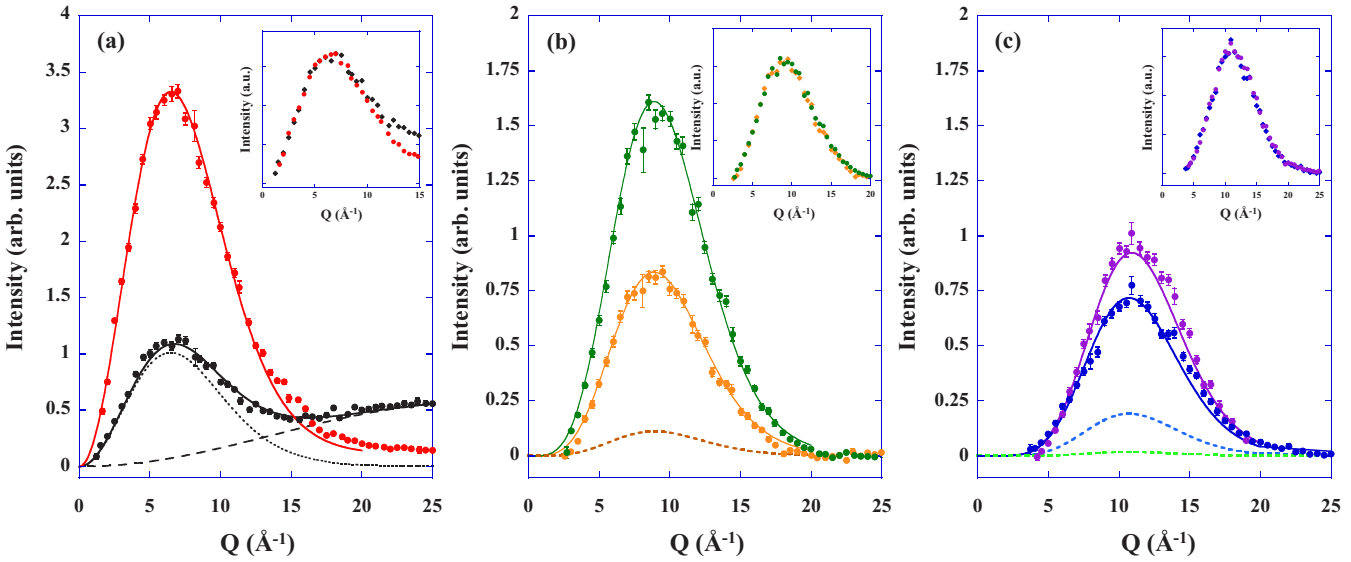

FIG. 3. Experimentally obtained $S(Q)$ spectrum sliced from the $S(Q,\omega)$ contour map in Fig. 1(a): (a) first excited states ($n = 1$) of 1K [60 meV (black circles)] and 1N [80 meV (red circles)]; (b) second excited states ($n = 2$) of 2M [140 meV (orange circles)] and 2N [160 meV (green circles)]; (c) third excited states ($n = 3$) of 3M [220 meV (blue circles)] and 3N [240 meV (purple circles)]. The theoretically fitted $S(Q)$ curves for each energy state are shown with solid lines. The theoretically calculated lowest-intensity triplet spectrum (dashed brown line) in (b) and the two lowest-intensity quadruplet spectra (dashed green and blue lines) in (c) are also included. The insets show the twin spectral characteristics of the two spectra for each energy state. The identical spectral shape is obtained by adjusting the peak intensity of the lower energy state to the magnitude for the higher energy state.

is degenerate. We describe the set of quantum numbers in the form of algebraic equations, as shown in the list of Table I. The theoretically estimated energies shown in Table I agree well with the experimentally observed energies, where the values of $\omega_{\nu\rho}$ are obtained by the normal mode analysis (see Supplemental Material S1 [40]). Therefore, the energy is equally separated between the first (1K and 1N), second (2M and 2N), and third (3M and 3N) energy states, and each state has two split levels.

Using the theoretically estimated energies shown in Table I, we can calculate the neutron-scattering spectrum intensity $S(Q)$ as a function of the magnitude of the momentum transfer Q. Figure 3 shows the experimentally obtained $S(Q)$ spectrum sliced from the $S(Q,\omega)$ contour map in Fig. 1(a) for (a) first excited states ($n = 1$) of both 1K [60 meV (black circles)] and 1N [80 meV (red circles)], (b) second excited states ($n = 2$) of both 2M [140 meV (orange circles)] and 2N [160 meV (green circles)], and (c) third excited states ($n = 3$) of both 3M [220 meV (blue circles)] and 3N [240 meV (purple circles)]. The peak intensity decreases, and the peak position shifts to higher Q values when the total quantum number $n = \sum_{\nu=1}^{2}\sum_{\rho=X}^{Z} n_{\nu\rho}$ increases. Furthermore, for a given total quantum number state, the spectral peak positions of both levels are at the same Q value. We show that these physical properties from the $S(Q)$ spectra in Fig. 3 can be quantitatively described by the scattering from the initial state to the final state. To obtain the theoretical $S(Q,\omega)$ curve, we use the Hermite orthogonal wave functions given in Eq. (4). The theoretical $S(Q,\omega)$ curve can be written as the absolute square of the transition matrix elements from the initial ground state $\Phi_0(\xi_{\nu\rho})$, to the final state $\Phi_{N_{\nu\rho}}(\xi_{\nu\rho})$, on the basis of the normal coordinate $\xi_{\nu\rho}$:

$$S(Q,\omega) = \left\langle \left| \sum_{\beta=1}^{2} b_\beta \prod_{\nu=1}^{2} \prod_{\rho=X}^{Z} \int \Phi^*_{n_{\nu\rho}}(\xi_{\nu\rho}) \times \exp\left(\frac{-i}{\sqrt{\mu_\beta}} Q_\rho \vartheta^{(\rho)}_{\beta\nu} \xi_{\nu\rho} \right) \Phi_0(\xi_{\nu\rho})\, d\xi_{\nu\rho} \right|^2 \right\rangle \times \delta\left[\omega - \sum_{\nu=1}^{2} \sum_{\rho=X}^{Z} n_{\nu\rho}\omega_{\nu\rho} \right], \quad (6)$$

where Q_ρ is the momentum-transfer vector component defined by $Q_\rho = k_\rho^{(i)} - k_\rho^{(f)}$, in which $k_\rho^{(i)}$ and $k_\rho^{(f)}$ indicate the wave vector components of the incident and scattered neutrons, respectively. In the above Eq. (6), b_β is the scattering length of each nucleus ($\beta = 1$ for Si and $\beta = 2$ for H) [24–26], and $\langle \cdots \rangle$ indicates the powder average [34,35], which represents the averaging of the absolute square of the transition matrix elements over the solid angle between $\mathbf{Q}$ and the displacement vector of each nucleus. Assuming that there is no correlation between the b values of different nuclei [24,25], $S(Q)$ becomes the sum of the three terms as $S(Q) = S^{\mathrm{H}}(Q) + S^{\mathrm{Si}}(Q) + S^{C}(Q)$, where the superscripts denote the scattering from H nuclei, Si nuclei, and their cross term, respectively. The theoretically evaluated cross-term scattering $S^C(Q)$ has a weaker intensity than the other scattering parts (see Supplemental Material S1 [40]); therefore, we can ignore the $S^C(Q)$ term, and we will consider the two $S^H(Q)$ and $S^{\mathrm{Si}}(Q)$ terms in order to fit the experimental results shown in Fig. 3.

By substituting $\Phi_{n_{\nu\rho}}$ in Eq. (4) into Eq. (6) and integrating with respect to each normal coordinate $\xi_{\nu\rho}$, and then taking the powder average, we can derive the theoretical $S^{\mathrm{H}}(Q)$ function as (see Supplemental Material S1 [40])

$$S^{\mathrm{H}}(Q) = \frac{\overline{(b_{\mathrm{H}})^2}}{4} Q^{2n} \exp\left[-\frac{Q^2}{2}\left\{\left(\Delta^{\mathrm{H}}_{1X}\right)^2 + \left(\Delta^{\mathrm{H}}_{2X}\right)^2\right\}\right] \times {}_1\overline{F}_1\left(\frac{1}{2} + n_{1Z} + n_{2Z}; \frac{3}{2} + n; \frac{1}{2}Q^2\left[\left(\Delta^{\mathrm{H}}_{1X}\right)^2 + \left(\Delta^{\mathrm{H}}_{2X}\right)^2 - \left(\Delta^{\mathrm{H}}_{1Z}\right)^2 - \left(\Delta^{\mathrm{H}}_{2Z}\right)^2\right]\right) \times \Gamma\left(\frac{1}{2} + n_{1X} + n_{2X}\right)\Gamma\left(\frac{1}{2} + n_{1Y} + n_{2Y}\right) \times \Gamma\left(\frac{1}{2} + n_{1Z} + n_{2Z}\right) \prod_{\nu=1}^{2}\prod_{\rho=X}^{Z} \frac{\left(\Delta^{\mathrm{H}}_{\nu\rho}\right)^{2n_{\nu\rho}}}{2^{n_{\nu\rho}} n_{\nu\rho}!}, \quad (7)$$

where $\overline{(b_{\mathrm{H}})^2}$ is the average values of the square of the scattering length for H, $n = \sum_{\nu=1}^{2}\sum_{\rho=X}^{Z} n_{\nu\rho}$, Γ denotes the gamma function, and ${}_1\bar{F}_1$ is the regularized hypergeometric function of the first kind, respectively.

In Eq. (7) above, the parameters $\Delta^{\mathrm{H}}_{1\rho}$ and $\Delta^{\mathrm{H}}_{2\rho}$ are given as

$$\left(\Delta^{\mathrm{H}}_{1\rho}\right)^2 = \left[\frac{\chi^2_{1\rho}}{\mu_2\left(\alpha^2_\rho + 1\right)}\right], \quad \left(\Delta^{\mathrm{H}}_{2\rho}\right)^2 = \left[\frac{\alpha^2_\rho \chi^2_{2\rho}}{\mu_2\left(\alpha^2_\rho + 1\right)}\right], \quad (8)$$

where α_ρ is the value obtained by the diagonalization procedure (see Supplemental Material S1 [40]).

The theoretical $S^{\mathrm{Si}}(Q)$ function is obtained by replacing the H superscript with Si as described in Eqs. (7) and (8). Note that $S^{\mathrm{Si}}(Q)$ exhibits a lower intensity in the spectrum than $S^{\mathrm{H}}(Q)$. For example, the spectral intensity of $S^{\mathrm{Si}}(Q)$ in the 1N state is less than ten times smaller than that in the 1K state, and $S^{\mathrm{Si}}(Q)$ has a significantly weaker spectral intensity than the higher energy states. Furthermore, the peak position of the $S^{\mathrm{Si}}(Q)$ spectrum is located in the region with greater transfer momentum Q than 25 $\mathrm{Å}^{-1}$. Therefore, we cannot observe the scattering from $S^{\mathrm{Si}}(Q)$ for higher energy states with the exception of the 1K state. The total theoretical scattering spectra (solid black line) composed of both $S^{\mathrm{H}}(Q)$ (dotted black line) and $S^{\mathrm{Si}}(Q)$ (broken black line) are plotted for the 1K energy state in Fig. 3(a). For the other spectra, we only consider the $S^{\mathrm{H}}(Q)$ term to fit the experimental results. To obtain the best fit of the experimental data shown in Figs. 3(a)–3(c), we use the following values: $\overline{(b_{\mathrm{H}})^2} = 6.53$ b, $\overline{(b_{\mathrm{Si}})^2} = 0.16$ b [26], $(\Delta^{\mathrm{H}}_{1X})^2 = (\Delta^{\mathrm{H}}_{1Y})^2 = 1.3 \times 10^{-2}$ Å^2, $(\Delta^{\mathrm{H}}_{1Z})^2 = 2.6 \times 10^{-3}$ Å^2, $(\Delta^{\mathrm{H}}_{2X})^2 = (\Delta^{\mathrm{H}}_{2Y})^2 = 4.2 \times 10^{-2}$ Å^2, $(\Delta^{\mathrm{H}}_{2Z})^2 = 1.5 \times 10^{-2}$ Å^2 (see Supplemental Material S1 [40]), and the Si:H stoichiometric ratio of 3:1, e.g., $S(Q) = S^{\mathrm{H}}(Q) + 3\,S^{\mathrm{Si}}(Q)$ is plotted for the $1K$ energy state. The stoichiometry is consistent with the size of n-Si (2.4 nm) [38,41]. This fact suggests that the scattering originates from the Si-H surface and the nanocrystalline Si core.

Finally, the hidden characteristics of the observed $S(Q)$ spectra were examined, and the two split levels at each energy state are shown to exhibit identical spectral shapes. This spectral shape was obtained by adjusting the peak intensity of the lower energy level to the magnitude of the higher energy level, as shown in the insets of Figs. 3(a)–3(c). These twin spectra directly prove that the vibrational dynamics are described by the harmonic oscillators of the normal modes. We consider the ratio of two scattering functions with the different energy levels, such as $S^{\mathrm{H}}(Q,n_{\nu\rho})$ and $S^{\mathrm{H}}(Q,n'_{\nu\rho})$. When the quantum numbers satisfy the conditions $\sum_{\nu=1}^{2}\sum_{\rho=X}^{Z}(n_{\nu\rho} - n'_{\nu\rho}) = 0$ and $\sum_{\nu=1}^{2}(n_{\nu Z} - n'_{\nu Z}) = 0$, which implies that the regularized hypergeometric function ${}_1\overline{F}_1$ takes the identical form for both $S^{\mathrm{H}}(Q,n_{\nu\rho})$ and $S^{\mathrm{H}}(Q,n'_{\nu\rho})$, we find that the ratio $\varpi\left(n_{\nu\rho}, n'_{\nu\rho}\right)$ can be expressed as

$$\varpi\left(n_{\nu\rho}, n'_{\nu\rho}\right) = \frac{\Gamma\left(\frac{1}{2} + n'_{1X} + n'_{2X}\right)\Gamma\left(\frac{1}{2} + n'_{1Y} + n'_{2Y}\right)\Gamma\left(\frac{1}{2} + n'_{1Z} + n'_{2Z}\right)}{\Gamma\left(\frac{1}{2} + n_{1X} + n_{2X}\right)\Gamma\left(\frac{1}{2} + n_{1Y} + n_{2Y}\right)\Gamma\left(\frac{1}{2} + n_{1Z} + n_{2Z}\right)} \prod_{\nu=1}^{2}\prod_{\rho=X}^{Z} \frac{n_{\nu\rho}!}{n'_{\nu\rho}!}\left(\Delta^{\mathrm{H}}_{\nu\rho}\right)^{2\left(n'_{\nu\rho} - n_{\nu\rho}\right)}. \quad (9)$$

Hence, the dependence on Q of the ratio will vanish. This similarity rule is the physical mechanism that gives rise to the twin spectra. The energy states of the identical total quantum numbers consist of twin spectral groups that are classified as the energy levels (first row) in Table I. An energy state with the total quantum number n is composed of the $n+1$ family. Therefore, the second and third excited states have triplet and quadruplet spectra. For example, the $n = 2$ state is composed of the 2K, 2M, and 2N spectral families, and the $n = 3$ state is composed of the 3K, 3L, 3M, and 3N spectral families. The ratio of these spectra, which obeys the similarity rule, is obtained by substituting the values given in Eq. (8) into Eq. (9) (see Supplemental Material S1 [40]). The comparison of the spectral intensity ratios between experimentally and theoretically obtained values is shown in Table I, where the ratios are normalized by the peak intensity of each N-level spectrum. In Figs. 3(b) and 3(c), the theoretically derived lowest-intensity triplet (2K) and two lowest-intensity quadruplet spectra (3K and 3L) are also described by the dashed lines. The corresponding experimental data are not available (2K, 3K, and 3L states) because the higher-order scattering intensities from the Si nucleus are too weak to observe.

In this work, we have shown the hidden quantum dynamics of hydrogen atoms that terminate the surface of n-Si using INS measurements. The twin spectral characteristics and similarity rule were elucidated based on the QDO model which described the cooperative motion of hydrogen and silicon. The duality elucidated in this work is likely not unique to n-Si but may also

be observed for other materials such as metal hydride alloys, which are important materials for use in hydrogen storage technologies [42,43].

We thank Professor Dai Hanawa for helping with our numerical simulation. T.M. thanks Professor Haruyuki Kusama and Professor Makoto Tomita for fruitful discussions.

[1] P. V. Gray and D. M. Brown, Appl. Phys. Lett. **8**, 31 (1966).
[2] J. I. Pankov and N. M. Johnson, *Hydrogen in Semiconductors* (Academic, New York, 1991).
[3] C. G. Van de Walle, Y. Bar-Yam, and S. T. Pantelides, Phys. Rev. Lett. **60**, 2761 (1988).
[4] C. Hu, S. C. Tam, F. C. Hsu, P. K. Ko, T. Y. Chang, and K. W. Terrill, IEEE Trans. Electron Devices **ED-32**, 375 (1985).
[5] I. -W. Wu, W. B. Jackson, T. -Y. Huang, A. G. Lewis, and A. Chiang, IEEE Electron Device Lett. **11**, 167 (1990).
[6] D. L. Staebler and C. R. Wronski, Appl. Phys. Lett. **31**, 292 (1977).
[7] M. Stutzmann, W. B. Jackson, and C. C. Tsai, Appl. Phys. Lett. **45**, 1075 (1984).
[8] Z. Zhou, L. Brus, and R. Friesner, Nano Lett. **3**, 163 (2003).
[9] T. Matsumoto, A. I. Belogorokhov, L. I. Belogorokhova, Y. Masumoto, and E. A. Zhukov, Nanotechnology **11**, 340 (2000).
[10] U. Gösele, Nat. Nanotechnol. **3**, 134 (2008).
[11] S. Godefroo, M. Hayne, M. Jivanescu, A. Stesmans, M. Zacharias, O. I. Lebedev, G. Van Tendeloo, and V. V. Moshchalkov, Nat. Nanotechnol. **3**, 174 (2008).
[12] K.-H. Kim, E. V. Johnson, A. G. Kazanskii, M. V. Khenkin, and P. R. Cabarrocas, Sci. Rep. **7**, 40553 (2016).
[13] Ch. Stuhlmann, G. Bogdányi, and H. Ibach, Phys. Rev. B **45**, 6786 (1992).
[14] P. Dumas and Y. J. Chabal, J. Vac. Sci. Technol. A **10**, 2160 (1992).
[15] P. Dumas, Y. J. Chabal, and G. S. Higashi, Phys. Rev. Lett. **65**, 1124 (1990).
[16] P. Jakob, Y. J. Chabal, Krishnan Raghavachari, and S. B. Christman, Phys. Rev. B **47**, 6839 (1993).
[17] Krishnan Raghavachari, P. Jakob, and Y. J. Chabal, Chem. Phys. Lett. **206**, 156 (1993).
[18] B. J. Min, Y. H. Lee, C. Z. Wang, C. T. Chan, and K. M. Ho, Phys. Rev. B **46**, 9677 (1992).
[19] B. Sandfort, A. Mazur, and J. Pollmann, Phys. Rev. B **51**, 7139 (1995).
[20] J. A. Appelbaum and D. R. Hamann, Phys. Rev. Lett. **34**, 806 (1975).
[21] R. Honke, P. Jakob, Y. J. Chabal, A. Dvořák, S. Tausendpfund, W. Stigler, P. Pavone, A. P. Mayer, and U. Schröder, Phys. Rev. B **59**, 10996 (1999).
[22] R. Honke, P. Pavone, and U. Schröder, Surf. Sci. **367**, 75 (1996).
[23] E. Fermi, Ric. Sci. **7**, 13 (1936).
[24] S. W. Lovesey, *Theory of Neutron Scattering from Condensed Matter* (Clarendon, Oxford, 1984).
[25] G. L. Squires, *Thermal Neutron Scattering* (Cambridge University Press, Cambridge, 1978).
[26] A. J. Dianoux and G. Lander, *Neutron Data Booklet* (Institut Laue-Langevin, Grenoble, France, 2003).
[27] W. Doster, S. Cusack, and W. Petry, Nature (London) **337**, 754 (1989).
[28] T. Yildirim, O. Gülseren, J.W. Lynn, C. M. Brown, T. J. Udovic, Q. Huang, N. Rogado, K. A. Regan, M. A. Hayward, J. S. Slusky, T. He, M. K. Haas, P. Khalifah, K. Inumaru, and R. J. Cava, Phys. Rev. Lett. **87**, 037001 (2001).
[29] A. D. Christianson, E. A. Goremychkin, R. Osborn, S. Rosenkranz, M. D. Lumsden, C. D. Malliakas, I. S. Todorov, H. Claus, D. Y. Chung, M. G. Kanatzidis, R. I. Bewley, and T. Guidi, Nature (London) **456**, 930 (2008).
[30] L. Hong, N. Jain, X. Cheng, A. Bernal, M. Tyagi, and J. C. Smith, Sci. Adv. **2**, e1600886 (2016).
[31] S. Ikeda, H. Sugimoto, and Y. Yamada, Phys. Rev. Lett. **81**, 5449 (1998).
[32] T.-C. Shen, C. Wang, G. C. Abeln, J. R. Tucker, J. W. Lyding, Ph. Avouris, and R. E. Walkup, Science **268**, 1590 (1995).
[33] E. T. Foley, A. F. Kam, J. W. Lyding, and Ph. Avouris, Phys. Rev. Lett. **80**, 1336 (1998).
[34] S. Ikeda, S. Kashida, H. Sugimoto, Y. Yamada, S. M. Bennington, and F. Fillaux, Phys. Rev. B **66**, 184302 (2002).
[35] S. Ikeda, M. Furusaka, T. Fukunaga, and A. D. Taylor, J. Phys.: Condens. Matter **2**, 4675 (1990).
[36] L. T. Canham, Appl. Phys. Lett. **57**, 1046 (1990).
[37] V. Lehmann and U. Gösele, Appl. Phys. Lett. **58**, 856 (1991).
[38] T. Matsumoto, J. Suzuki, M. Ohnuma, Y. Kanemitsu, and Y. Masumoto, Phys. Rev. B **63**, 195322 (2001).
[39] R. Hull, *Properties of Crystalline Silicon* (INSPEC, The Institution of Electrical Engineering, London, UK, 1999).
[40] See Supplemental Material at http://link.aps.org/supplemental/10.1103/PhysRevMaterials.1.051601 for details on the twin spectral calculation.
[41] T. Uda and M. Hirao, Surf. Sci. **306**, 87 (1994).
[42] N. L. Rosi, J. Eckert, M. Eddaoudi, D. T. Vodak, J. Kim, M. O'Keeffe, and O. M. Yaghi, Science **300**, 1127 (2003).
[43] L. Schlapbach and A. Züttel, Nature (London) **414**, 353 (2001).